Athermal evolution of nanocrystalline tungsten driven by irradiation

Pui-Wai Ma *, Daniel R. Mason, Steven Van Boxel, Sergei L. Dudarev

United Kingdom Atomic Energy Authority, Culham Science Centre, Abingdon, Oxfordshire, OX14 3DB, United Kingdom

A R T I C L E   I N F O

A B S T R A C T

Radiation effects in nanocrystalline tungsten are simulated in the athermal high dose limit, where microstructural evolution is driven not by the thermally activated diffusion of radiation defects, but by the fluctuating stress field resulting from the production and relaxation of defects. Over a large interval of exposure spanning several dpa, samples with smaller grains swell less than those with larger grains, featuring defect denuded zones resulting from the continuously fluctuating atomic configurations at grain boundaries. The grain size distribution broadens as a function of exposure, with the average grain size increasing, subject to the visibility criterion applied to the identification of small grains. This work makes a quantitative analysis of how the dynamic recombination of defects in the grain boundary region, responsible for the known superior radiation resistance of nanocrystalline materials, emerges spontaneously in atomistic simulations.

1. Introduction

High-energy neutrons, generated by the nuclear fuel in a fission reactor or by the deuterium-tritium plasma in a fusion device, undergo multiple scattering by the atomic nuclei and propagate over several tens of centimetres in reactor materials [1]. Elastic and inelastic interactions of energetic neutrons with atomic nuclei generate γ-radiation [2] and atomic recoils [3], where the latter initiate collision cascades that in a perfect crystal produce readily identifiable structural defects, primarily dislocation loops and vacancy clusters [4–6]. The accumulation of these defects degrades thermal [7–9] and mechanical [10,11] properties of materials, giving rise to swelling [12,13] and dimensional changes [14]. The fact that microstructurally complex materials exhibit greater stability under irradiation is well recognised. For example, ferritic-martensitic steels show far greater resistance to radiation swelling than alloys with similar chemical compositions [13,15,16].

Nanocrystalline (NC) materials are a notable class of materials with complex microstructure, characterised by a large grain boundary (GB) interface to volume fraction [17]. The recognition of a potentially beneficial role of GBs stimulated research in nanostructural materials exposed to irradiation [18–20]. At high temperatures, defects migrate by thermal activation and are absorbed and annihilated at GBs [21,22], resulting in the formation of zones of lower defect density near GBs often observed experimentally [22,23]. The average density of radiation

defects in NC and ultra-fine grained materials is lower than in coarse-grained samples exposed to the same radiation dose [19,24]. This is observed in NC metals and insulators [25,26], suggesting that the defects production suppression effect is generic and associated solely with the high density of GBs. Mathematical analysis of the interaction of defects with GBs, where the latter are represented by dislocation arrays and where defects are assumed to perform thermally activated diffusion [27], has gone some way to explain the variation of the density of defects as a function of the average grain size.

Atomic scale simulations help understand the nature of the interaction between an individual GB and radiation defects [28–36]. GBs are often considered as strong sinks for radiation defects [18,28,29,32], especially for the self-interstitial atom (SIA) type defects. But simulations show that a GB is not a static sink for defects but rather a dynamically evolving region, altering its configuration in the process of absorption or emission of a defect. A GB can even emit SIA defects to annihilate vacancies nearby [29], and the annihilation of defects at a GB itself is a collective process, involving the rearrangement of positions of many atoms [32]. The fluctuating motion of GBs in copper under irradiation [30,31] results in that the stacking fault tetrahedron (SFT) defects are incorporated into GBs through collective many-body reactions.

Fluctuations of GB structures, whether thermal or athermal - i.e. driven solely by irradiation - are expected to coarsen the grain microstructure [37]. The coarsening of grains under irradiation was ob-

---

* Corresponding author.

E-mail addresses: Leo.Ma@ukaea.uk (P.-W. Ma), Daniel.Mason@ukaea.uk (D.R. Mason), Steven.Van.Boxel@ukaea.uk (S. Van Boxel), Sergei.Dudarev@ukaea.uk (S.L. Dudarev).

served experimentally [38,39,37,40]. Initially, Wang et al. [38] assumed that the average diameter of grains varied linearly as a function of radiation exposure. Further studies showed that at high doses, the rate of grain growth slows and becomes sub-linear [39,40]. Kaoumi et al. [37] developed a qualitative model, based on Vineyard's thermal spike concept [41], predicting that in the temperature-independent regime, the variation of the average grain size $\bar{d}_g$ as a function of dose ϕ follows a cubic polynomial law $\bar{d}_g^{\,3}(\phi) - \bar{d}_g^{\,3}(0) \propto \phi$. This functional form appears to provide a good fit to the available experimental data, but it has not yet been examined if the model is consistent with direct simulations.

Below, we simulate microstructural evolution and evaluate the swelling of heavily irradiated NC tungsten in the athermal limit using the creation-relaxation algorithm (CRA) [42]. As a part of this study, we show how to construct two-dimensional surfaces separating grains. This then provides a measure of distance from a grain boundary that we can use to plot defect properties as a function of distance to the nearest GB plane. By extending the simulations into the interval of high dose, previously inaccessible to direct computational analysis, we find that in the athermal limit, the relationship between the grain size and swelling rate stems from the reduction of defect content in the vicinity of GBs. We explore the fluctuating dynamics of GBs under radiation exposure, and find that the presence of a GB nanostructure slows down the rate of evolution of microstructure, which nevertheless appears to tend towards a dynamic driven steady state [42–44]. Direct simulations also show that thermally activated diffusion is not the only mechanism responsible for the experimentally observed formation of defect denuded zones near GBs, which in our simulations emerge as a result of stress-driven fluctuations of the GB atomic structure. Irradiation-induced defects are absorbed and incorporated into GBs, which continuously alter their morphology, leading to grain coarsening. Therefore, GBs behave as dynamically evolving structures rather than static sinks for radiation defects.

2. Generating atomic configurations characteristic of high dose irradiation in NC tungsten

Simulation cells with equiaxed grains were generated using the Voronoi tessellation method using the ATOMSK code [45]. Voronoi polyhedra are filled with atoms in a body-centred-cubic (bcc) structure with random crystallographic orientations. ATOMSK then removes atoms until none has a neighbour within 2 Å. We created six sets of simulation cells. Four out of six are initialised with characteristic grain diameters, d_c, of 5.0, 7.5, 10.0, and 12.7 nm in a cubic cell with a cell side length of 25.144 nm. Their volumes are equivalent to those of a cubic cell containing $80 \times 80 \times 80$ bcc unit cells. The other two sets are initialised with d_c of 15.1 and 20.4 nm in a cubic cell with a cell side length of 37.716 nm. Their volumes are equivalent to a cubic cell containing $120 \times 120 \times 120$ bcc unit cells. The initial characteristic grain diameter d_c is the diameter of a sphere with the same volume as an average grain. We also created cells with perfect crystal structures. The quantitative results shown below are averaged across five independent samples from each set of simulations.

Our preparation method for relaxing the NC starting configurations is similar to that described in Ref. [42]. First, we relax an atomic configuration using conjugate gradients, followed by thermal relaxation at 300 K for 1 ns. Then, we allow the cells to change their volumes and shapes to achieve stress-free conditions, and run MD simulations for a further 1 ns. The temperature is linearly reduced from 300 K to 0 K during the second stage of the simulation. Finally, the cell and atomic configuration are relaxed using the conjugate gradients again. All the simulations were performed using LAMMPS [46,47], and the Marinica EAM4 [48] as well as the Mason-Nguyen-Manh-Becquart (MNB) interatomic potentials [49]. The results are qualitatively similar, exhibiting some quantitative differences, where typically a more dense defect distribution is found using EAM4, in agreement with other

studies [50,51,42]. The MNB potential predicts the low-energy defect structures and formation energies with high accuracy [49]. The data for dislocation loops and voids derived from simulations performed using the MNB potential agree well with DFT and elasticity predictions [52]. For the clarity of exposition, in what follows we only show the results produced using the MNB potential.

The evolution of the microstructure of an NC material in the high dose limit is explored using a parameter-free atomistic CRA simulation [42]. We use the canonical displacements per atom (cDPA) units to characterise the dose and distinguish it from the conventional definition of NRT-DPA [53]. A Frenkel pair is created by moving a randomly selected atom to a random position. At each CRA step, we create n Frenkel pairs, and the resulting atomic configuration is then relaxed using the conjugate gradient energy minimisation. This accumulates the dose of n/N cDPA at each simulation step [42], where N is the total number of atoms in the simulation cell. At each step, atomic configurations evolve according to the current spatially heterogeneous energy landscape formed by the execution of the preceding steps of the algorithm. The shape and volume of the simulation cell are also relaxed to stress-free conditions. Further details of the simulation methods are provided in the Supplementary Material.

In the initial implementation of the CRA algorithm [42], a single Frenkel pair was generated per algorithmic step ($n = 1$). Subsequent studies [54,55,43] have demonstrated that in large simulation cells, displacing multiple atoms per cycle does not affect the overall results, and is more computationally efficient. These latter studies used a rate of approximately 0.001 cDPA per cycle or larger. In the simulations below, we accumulate 0.001 cDPA per algorithmic cycle and repeat these cycles until the desired dose is achieved.

Chartier and Marinica [56] performed Frenkel Pair Accumulation (FPA) simulations of iron, using an algorithm that shares conceptual similarities with the CRA. The FPA simulations were performed at 300 K and hence included some thermal effects whereas the CRA focuses solely on the evolution driven by lattice deformations. The patterns of evolution deduced from both simulations are consistent [42], and the predicted microstructures also agree with experimental observations by Wang et al. [44]. Remarkably, the microstructures observed experimentally in [44] are similar to those predicted by simulations irrespective of the fact that experiments were performed at room temperature and hence included the effects of thermally activated diffusion of SIA defects that in tungsten are mobile at temperatures as low as 27 K [57,58].

3. Identifying grain boundaries from atomic positions

In this work, we want to characterise defect concentrations as a function of distance from the nearest grain boundary. Hence we start by summarising the algorithms used for determining whether an atom is in a particular grain, and how we find its distance to a GB.

The assignment of a grain index to each atom is adapted from the DBSCAN algorithm [59], and considers the orientation mismatch between each atom and its near neighbours. This assignment algorithm has four stages.

1. The crystal lattice orientation is determined for each atom. If we write the expected position of the kth neighbouring atom in the perfect lattice as $\mathbf{x}_k^0$, and the observed position as $\mathbf{x}_k$, we can minimise a fitting function $S = \sum_k (\overline{\mathbf{T}}\mathbf{x}_k - \mathbf{x}_k^0 - \delta)^2$ with respect to the components of the deformation gradient matrix $\overline{\mathbf{T}}$ and the vector displacement δ. While this algorithm is known to be less efficient than the graph-based Polyhedral Template Matching algorithm [60] in a perfect crystal, it is more robust when there are many lattice defects. We choose to fit to the expected neighbour positions within 1.5 lattice parameters (between the third and fourth nearest neighbour shells for bcc). We interpret the deformation gradient as a stretch and rotation, $\overline{\mathbf{T}} = (1 + \overline{\varepsilon})\overline{\mathbf{R}}$ using the polar decomposition method, and find a quaternion representing the local lattice rotation $\overline{\mathbf{R}}$.

2. Regions where clusters of atoms have similar orientations to their neighbours are identified. These regions are the grain interiors. The quaternion distance between two neighbouring atoms, $d = 1 - (q_1 \cdot q_2)^2$, gives the angle of rotation, θ, between two atom orientations as $\cos\theta = 1 - 2d$. Each atom for which $\theta < \theta_c$ for every neighbour is in a (locally) crystalline region. These are clustered so a pair of atoms within a distance r_c of each other in a crystalline region are assigned to the same grain, g, if the angle between them $\theta < \theta_c$. We choose $\theta_c = 5°$ and $r_c = 1.1$ lattice parameters. Atoms without similar orientation neighbours form an unsorted pile.

3. The atoms in the unsorted pile are adopted into grains where possible. We first return to the pile any atom already assigned to grain g if the majority of its neighbours (distance within r_c) are in a different grain g'. Then we assign any atom on the pile to grain g if it has a close orientation ($\theta < \theta_c$) to a majority of neighbours already in grain g. Finally, we assign any atom on the pile to grain g if it has a simple majority of neighbours already in grain g.

4. We return all atoms in a grain with fewer than N_{min} atoms to the pile. We choose $N_{min} = 100$. This process of unassigning and reassigning to adopt atoms into grains is iterated until a stable grain distribution is found. Some atoms will never be assigned to a grain if no majority can be found. In this work, we find that typically much fewer than 1% of atoms are left unassigned, and we find no evidence of amorphous regions.

While the algorithm above will place nearly all atoms into grains, even when there is a large number of lattice defects, it does not define grain *boundaries*. We use the definition that a GB is a hypothetical surface dividing two crystalline regions with different orientations. This definition does not preclude the possibility that there exists a volume near the surface which is amorphous, nor does it preclude a void or a precipitate straddling the GB. If a GB is so defined, then a computationally efficient representation of it is a triangulated surface. Using a triangulated surface, the subsequent calculations we need - the volume enclosed, the area, and the distance of a point to the surface - are well defined.

To identify the location of GB surfaces, we start with the atom positions and their assigned grain indices, found above. We then define a regular spaced node lattice with spacing L chosen to be greater than the lattice parameter and smaller than the expected radius of curvature of the grains. For this work, we chose $L = 5$ Å, and found that the result is insensitive to the exact choice of L. Each node is at the centre of a cell containing several atoms. We consider the positions and grain index of all atoms within the neighbouring 27 cells of a node point. For each pair of grains, g and g', we fit a smooth phase profile $\phi_{g,g'}(\mathbf{x}) = \tanh(\mathbf{x} \cdot \mathbf{b}_{g,g'} + a_{g,g'})$, which minimises the function $\tilde{S} = \sum_{g_i = g} (\phi_{g,g'}(\delta\mathbf{x}_i) + 1)^2 + \sum_{g_i = g'} (\phi_{g,g'}(\delta\mathbf{x}_i) - 1)^2 + \left(\frac{1}{|\mathbf{b}_{g,g'}|} - L\right)^2$, where $\delta\mathbf{x}_i$ is the vector from the node to atom i. This fitting returns a vector $\mathbf{b}_{g,g'}$ normal to the GB locally, oriented such that $\phi_{g,g'} = -1$ in grain g, and $\phi_{g,g'} = +1$ in grain g'. The last term in the fitting function stops the interface from becoming infinitely sharp. The position across the $g - g'$ GB at the node point is $\phi_{g,g'}(\mathbf{0}) = \tanh(a_{g,g'})$.

With the phase parameter position across each of the GBs computed at each node, the extent to which the node is in grain g is the value $\phi_g = \min(\{\phi_{g,g'}\})$, which takes the value -1 for a point deep inside grain g, and the value $+1$ for a point far outside grain g. We can (tri)linearly interpolate this function to find a phase field at every point in space, such that $\phi_g(\mathbf{x})$ returns the correct values on the nodes, and so a triangulated surface for the boundary of grain g can then be found as the isosurface $\phi_g(\mathbf{x}) = 0$ using the Marching Cubes algorithm [61,62].

An illustration of the result of this method is shown in Fig. 1. We can see a few GB atoms and defects with local lattice orientations proving difficult to identify, but a near-constant orientation in grains is produced by the method described above. One grain is shown as a triangulated surface, within which vacancies are drawn using the iso-
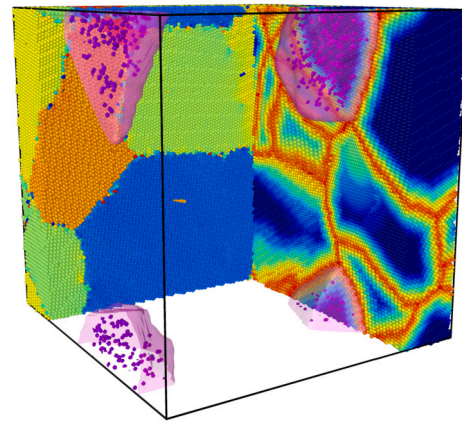
Fig. 1. A nanocrystalline sample ($d_c = 10.0$ nm) at dose 2.5 cDPA analysed using the methods described in the text. Atoms on the back left face are coloured by orientation. Atoms on back right face are coloured by distance to grain boundary. The pink surface shows the triangulated surface constructed for one grain, and the purple surfaces show voids within this grain. Image rendered using data exported to OVITO [64]. (For interpretation of the colours in the figure(s), the reader is referred to the web version of this article.)

surface method of Ref. [63]. Note that a zone denuded of vacancies is also clearly visible.

4. Results and discussion

Fig. 2 illustrates one of the main findings derived from our simulations of NC materials, showing that samples with smaller grains appear more resistant to radiation-induced swelling. The figure shows the variation of the average atomic volume and relative volume of systems with various initial grain sizes as a function of dose. The perfect crystal case is also shown for comparison. Samples with smaller grains have a larger volume per atom prior to irradiation, where the initial excess volume is due to the non-crystalline arrangement of atoms in the GBs. The volume of the sample, i.e. the volume of the entire simulation cell, increases as defects accumulate. At high doses, the relative increase is lower for the smaller grain samples. An examination of the relative volume change of the simulation cell shows that systems with smaller grain sizes exhibit lower swelling than samples with initially larger grains or single crystals.

Fig. 2 also illustrates an important, and well-known, effect of delayed microstructural evolution of a nanostructural material under irradiation in comparison with a material with simple microstructure. Experiments [13,15] show that over a certain initial interval of dose, steels exposed to irradiation exhibit almost no dimensional change or swelling. Subsequently, after a certain "incubation" dose, the rate of swelling of steels approaches that of simple alloys, showing that it is the initial nanostructure of the material that is responsible for the observed resistance to irradiation. The bottom panel of Fig. 2 illustrates this phenomenon, showing that a nanostructural material with an average smaller grain size evolves more slowly towards the asymptotic high dose driven steady state of the material [42,44] than a single crystalline or a large grain size system.

The origin of radiation resistance of a fine grain nanostructure stems from a combination of contributions from the variation of the total GB area and vacancy & void (v + v) content.

First, we examine the effect of the total GB area. Fig. 3 shows a sample with initial $d_c = 7.5$ nm at different radiation exposures. Both the defect content and GB nanostructures evolve and change significantly as a function of dose, graphically illustrating that GBs do not represent static sinks for defects that remain stationary in real space, as it is sometimes assumed in literature [65]. GBs interact with defects, evolve, and fluctuate. Grains change shape and coarsen as the dose increases. Rendering the orientation of the atoms using polyhedral template matching
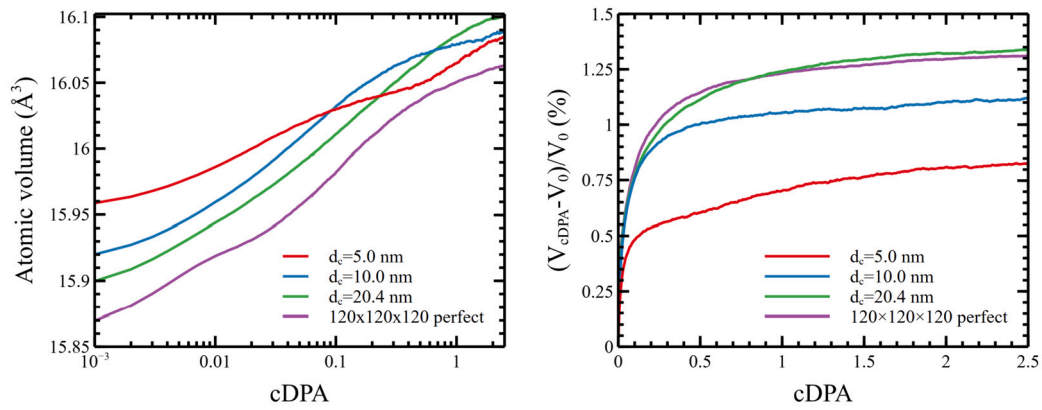
Fig. 2. Variation of the average atomic volume, and the relative volume of the simulation cell defined with respect to its initial volume, as functions of dose, expressed in cDPA units.
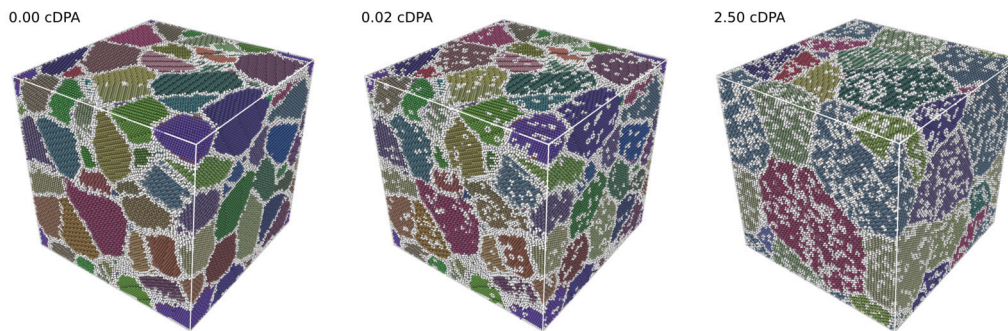
Fig. 3. A nanostructural sample, initially containing 71 grains with $d_c = 7.5$ nm, shown at different radiation exposures defined by the cDPA parameter. Crystal structures and crystal orientations are determined using the polyhedral template matching algorithm [60]. Atoms are coloured according to their local crystal orientation. Atoms in a non-bcc environment are shown as white.
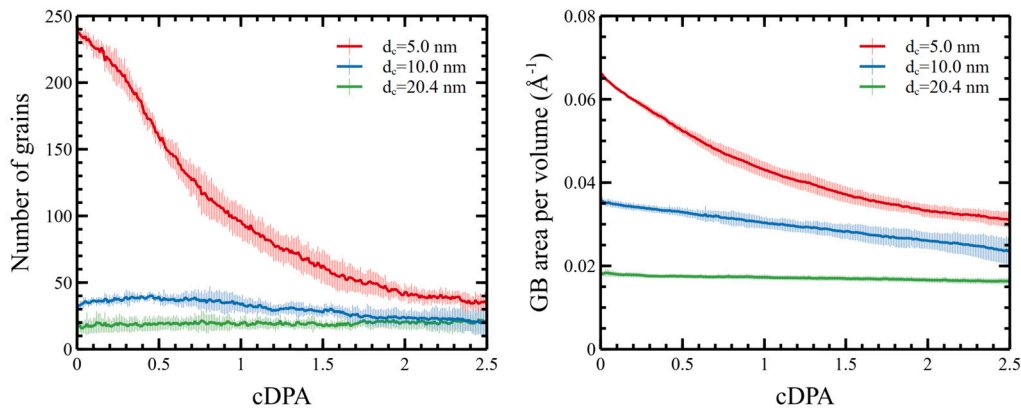
Fig. 4. Number of grains and grain boundary area per unit volume as a function of dose. Error bars are the standard deviation defined across the five samples.

in Fig. 3 highlights the increasing number of non-bcc atoms both at the grain boundary and at lattice defects, and could be compared to our analysis of the grains in Fig. 1.

Our simulations are consistent with the studies by Levo et al. [66], who performed collision cascade MD simulations of NC nickel and nickel-based multi-components alloys with a grain size of 10 nm, observing similar grain coarsening. Our results also agree with Refs. [18,28–32] showing that GBs interact with defects and change morphology as a result of local atomic rearrangement of their structure.

To examine the changing number of grains and the total GB area quantitatively, we plotted them in Fig. 4 as a function of dose. For the smaller grain samples, the number of grains decreases rapidly as a function of dose, whereas the samples with larger grains show a markedly lower decrease in the grain count. All the samples exhibit

grain coarsening, where the GB area per unit volume decreases significantly, especially if the initial grain size is small. Therefore, the excess volume due to the presence of GBs in the sample decreases. This is the first phenomenon countering the increase of the average atomic volume due to the accumulation of defects.

Do the grains really coarsen? The variation of grain size distribution can be quantified similarly to how it was done in Refs. [37,40] by plotting a histogram of grain sizes, see for example Fig. 5. The corresponding density map is shown in Fig. 6. The grain diameter d_g is evaluated from each grain volume in the spherical shape approximation [37]. For systems with the initial grain size of $d_c = 5.0$ nm, a clear pattern of grain coarsening is observed. For samples with the initially larger grains, the grain size distributions exhibit broadening instead. Not only larger grains can be observed at doses above 1.0 cDPA, small
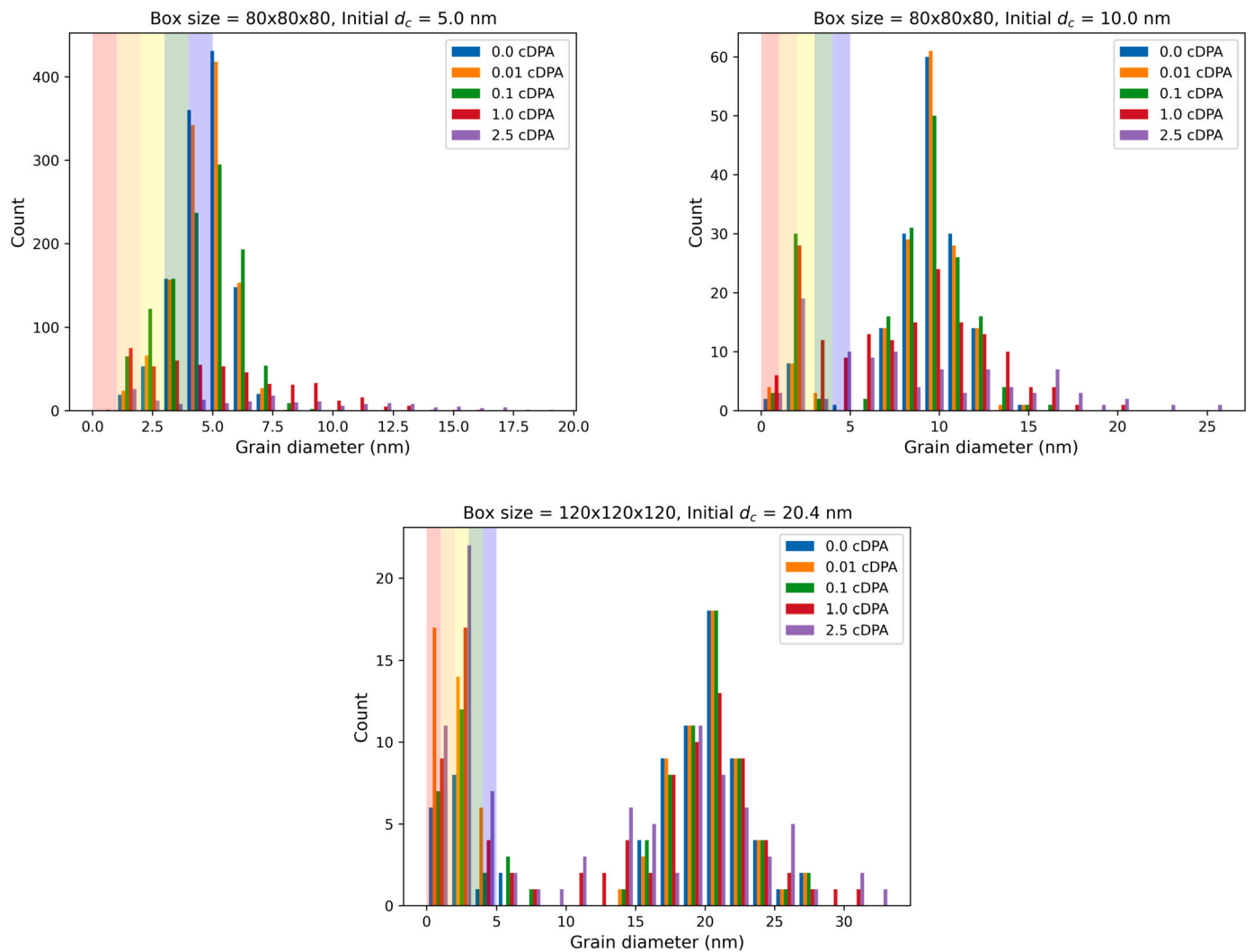
Fig. 5. Histogram of grain diameters at various exposures to radiation, where the dose is defined by the canonical DPA (cDPA) parameter. Grain diameters are computed from the grain volume in the spherical grain approximation. Shaded areas refer to varying levels of grain visibility.

grains also form at high doses. A grain is often defined as a group of atoms with neighbourhoods sharing similar crystal orientation, while in our algorithm we use a cutoff of 100 atoms as the smallest size of a grain, corresponding to $d_g \approx 1.4$ nm. It is not unlikely that the high number of grains with $d_g < 1.4$ nm stems from the very small fragments produced by irradiation that collectively appear as small grains. On the other hand, we also observe a greater number of small grains with d_g in the size range from 2 to 5 nm.

By inspecting the histograms summarising the results of ion irradiation [39,40] and neutron irradiation [67] experiments, one can define the visibility limit of grains at about $d_g = 5$ nm. Below this size, grains cannot be unambiguously identified due to the limitations of experimental imaging techniques. We shaded the histogram of grain sizes derived from simulations by different colours at 1 nm increments. As the visibility decreases, small grains are gradually eliminated from the analysis. This procedure recovers the size distribution generally observed in experiments where only large grains are identified. Although numerous small grains are present in the samples, for the initial size $d_c \geq 10.0$ nm, the total volume of grains smaller than 5 nm at all doses is lower than 1% of the total. In the actual observations, such small grains are easily confused with a part of the GB structure and ignored.

Grain coarsening implies the increase of the average grain diameter as a function of radiation exposure. Ion irradiation experiments [68] suggest that the average grain diameter varies with dose as

$\bar{d}_g{}^n(\phi) - \bar{d}_g{}^n(0) \propto \phi$, where $1.9 < n < 4.3$. Kaoumi et al. [37] developed a thermal spike model that predicts $n = 3$, in agreement with experimental observations. Experimental data on neutron-irradiated NC copper [67] also exhibit a sublinear increase of $\bar{d}_g$ as a function of dose. Our analysis suggests that the grain visibility limitations involved in the interpretation of experimental observations or the choice of the cutoff diameter in a simulation affect the counting and identification of grains. The average grain diameter is a quantity that depends on one's subjective interpretation. The thermal spike effect, which causes local heating, is not considered in CRA simulations, making a direct comparison to Kaoumi et al.'s model not appropriate. Additional analysis on the variation of grain diameters as a function of dose can be found in Supplementary Material.

Other than grain coarsening, the interaction of defects with GBs affects the production of defects, especially the v + v content, resulting in the lower radiation swelling of NC samples in comparison with single crystalline or large grain size samples. Interpreting the dependence of swelling on the grain microstructure requires analysing the spatial distribution of defects in the presence of GBs. The algorithm described in section 3 generates an instantaneous configuration of GBs as a triangulated surface. A distance from an atom to each triangle can be computed, enabling the definition of the minimum distance from an atom to a GB. Using this measure, various parameters can be defined and plotted as a function of distance to a GB.
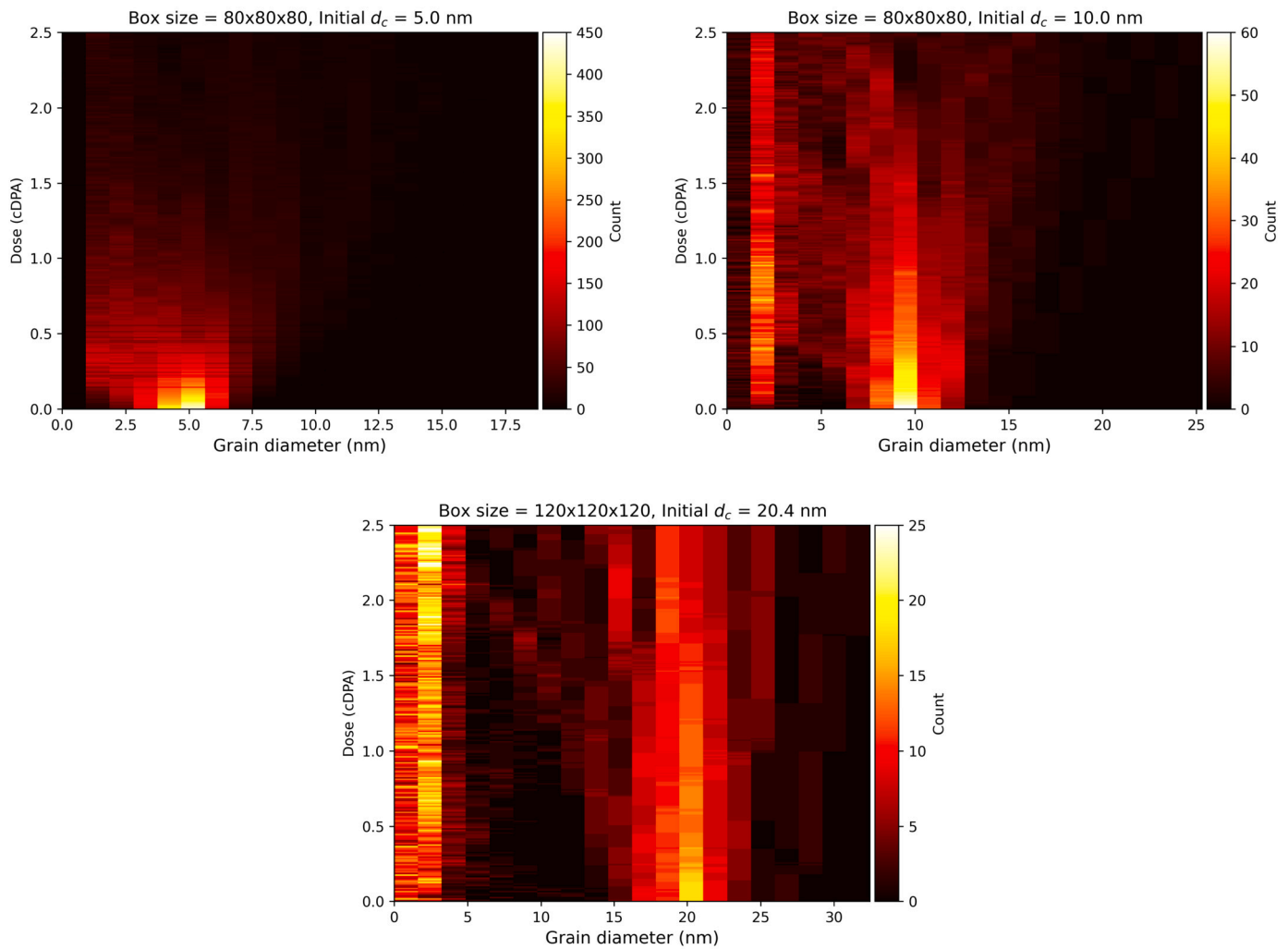
Fig. 6. Density map of grain diameters at various exposures to radiation, where the dose is defined by the canonical DPA (cDPA) parameter. Grain diameters are computed from the grain volume in the spherical grain approximation.
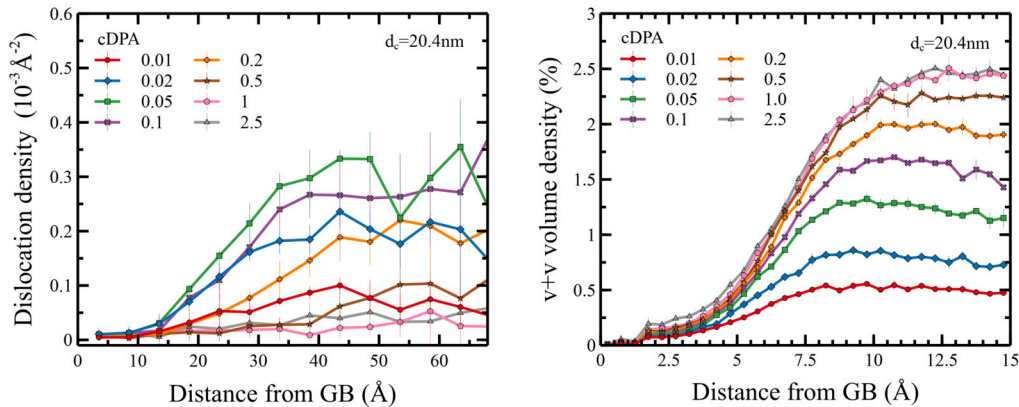
Fig. 7. Dislocation density and void and vacancy (v + v) volume density plotted as functions of the distance from a grain boundary. A detailed account of the method used for evaluating the v + v volume density is given in the Supplementary Material.

Fig. 7 shows the dislocation density and v + v volume density as a function of distance from a GB. The definitions used in the Figure are detailed in the Supplementary Material. The majority of dislocation lines have the Burgers vectors $\mathbf{b} = \frac{1}{2}\langle 111 \rangle$ and $\langle 100 \rangle$, and the proportion of dislocations with $\mathbf{b} = \langle 110 \rangle$ Burgers vectors is negligible. Both the dislocation density and the v + v content are lower near GBs, exhibiting a clear signature of a defect-depleted "denuded" zone [22]. Since the presence of vacancies and voids is associated with radiation swelling, the occurrence of zones with a lower vacancy and void content implies that the total v + v content in a nanostructure is lower than in a perfect crystal near the GBs. This is the second aspect of microstructural evolution making NC materials more irradiation swelling resistant.

Prior to conducting a dislocation analysis, we need to exclude atoms close to the GB, because a low angle GB can be considered as an array of
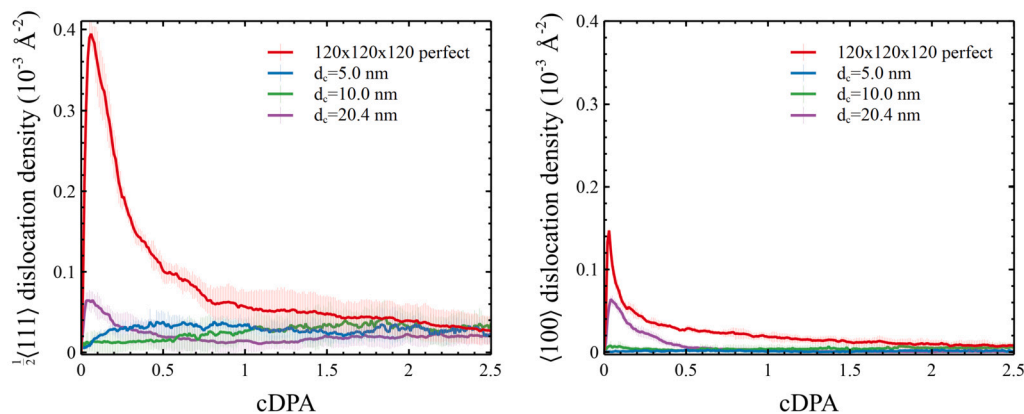
Fig. 8. Density of dislocation with Burgers vector $\mathbf{b} = \frac{1}{2}\langle 111 \rangle$ and $\langle 100 \rangle$ as a function of cDPA.
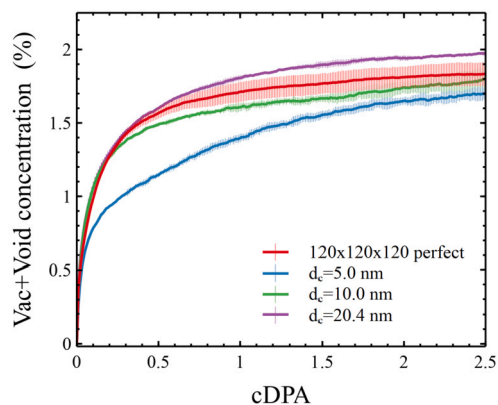
Fig. 9. Vacancy and void concentration as a function of cDPA.

dislocations. We excluded atoms with distances less than 1 Å from a GB. Fig. 8 illustrates that the dislocation density associated with the Burgers vector $\mathbf{b} = \frac{1}{2}\langle 111 \rangle$ is higher than that of $\langle 100 \rangle$. This finding agrees with the results of TEM experiments conducted by Yi et al. [69] on tungsten under self-ion irradiation. Importantly, simulations show that the presence of the initial NC structure suppresses the accumulation of dislocation density at low doses.

Fig. 9 illustrates a relationship between the variation of the v + v volume and cDPA. The v + v volumes observed in a perfect crystal exhibit a quantitative trend similar to that found in simulations conducted by Derlet and Dudarev [42]. Materials with small and medium grain sizes tend to display lower v + v volumes. Interestingly, an NC sample with $d_c = 20.4$ nm exhibits a higher v + v volume fraction than a perfect crystal at high doses. The origin of this phenomenon remains unclear. From the examination of Fig. 2, we conclude that the relative volume change of a large grain system and a perfect crystal are similar. This appears to suggest that the decrease of excess volume due to GBs opposes the increase of the v + v volume here. Even though the microstructures are different, the swelling values are not dissimilar.

What is the origin of defect denuded zones in the absence of diffusion and what is the mechanism of grain coarsening driven by irradiation? These two seemingly different questions reflect two manifestations of the same physical phenomenon. Both result from the fluctuating movement of GB structures due to irradiation and from GB-defect interactions. When GBs and defects interact, since both represent higher energy atomic structures, a lower energy configuration is attained as a result of relaxing the atomic environment. Local lattice distortions, associated with high stress concentrations, drive the rearrangement of atomic configurations [42,54,55,43,70]. Defects near a GB are absorbed and incorporated into the GB, changing its morphology, and the process itself has a clear signature of a local structural fluctuation.

Fig. 10 shows snapshots of the von Mises stress (VMS), illustrating the evolution of a nanostructural sample over the dose interval from 2.515 cDPA to 2.520 cDPA. Each figure corresponds to the dose increment of 0.001 cDPA. At the bottom of the first few frames, we see a large defect, corresponding to atoms with high VMS. In the later frames, this high stress region is relaxed. The atomic configuration of the defect is strongly perturbed by a small increment of dose. This destabilises the defect structure, enabling the atoms to rapidly reconfigure into a locally lower stress configuration. Given the simulation methodology, it would be incorrect to conclude that an interstitial defect cluster has diffused towards, and has been absorbed by a GB 'sink', in this sequence of images. Instead, it is appropriate to say that the local atomic configuration rearranged and attained a lower stress - lower energy state.

This sequence of images also shows that interfaces between the relatively disordered high-energy-per-atom and relatively perfect crystalline regions act as regions catalysing the recombination of defects. GBs do *not* act as static sinks for defects, as was assumed in Ref. [65]. Instead, they are dynamic fluctuating catalysts for recombination and structural relaxation of defects generated by irradiation, capable of slowing down the accumulation of radiation effects even in the absence of diffusion. This study provides insight into the microscopic processes of interaction and relaxation driving the complex evolution of nanostructures under irradiation.

5. Conclusions

By direct atomic scale simulations, we show that nanocrystalline tungsten is more resistant to the effects of irradiation-induced swelling than a single crystalline material. Simulations describe the limit of high dose and low temperature conditions, where a single crystalline material has recently been extensively explored theoretically [42] and experimentally [44]. Irradiation generates lattice defects that GBs can absorb and incorporate through continuous fluctuating rearrangement of local atomic configurations, leading to the formation of defect denuded zones. This also changes the GB morphology, resulting in grain coarsening. The average defect concentration is lower in a small grain size nanostructure, correlated with a higher relative volume of denuded zones. The relative volume increase is also lower due to the higher initial volume of the material containing high GB density, explaining the lower radiation swelling observed in NC materials. In a remarkable departure from predictions derived from simulations and observations of single crystalline materials [42,44], we do not attain a dynamically fluctuating steady state in an NC tungsten within 2.5 cDPA, illustrating a critically significant role of transient changes associated with GB structures slowing down the accumulation of defects in a nanostructural material. Concluding the narrative, we note that thermal effects at GBs in materials exposed to a high irradiation dose warrant further investigation.
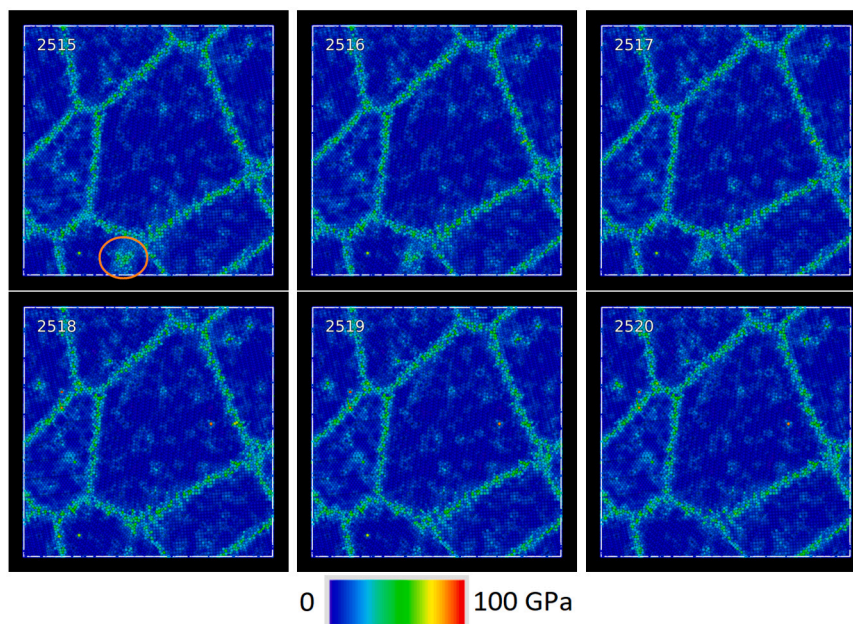
Fig. 10. Spatial distribution of the von Mises stress in a nanostructural sample with initial $d_c = 10.0$ nm, evolving in the interval of dose from 2.515 to 2.520 cDPA, corresponding to the CRA steps from 2515 to 2520. A defect cluster at the bottom of the figure is absorbed by the nearest GB.

CRediT authorship contribution statement

Pui-Wai Ma: Conceptualization, Data curation, Formal analysis, Investigation, Methodology, Software, Visualization, Writing – original draft, Writing – review & editing. **Daniel R. Mason:** Conceptualization, Formal analysis, Methodology, Software, Visualization, Writing – original draft, Writing – review & editing. **Steven Van Boxel:** Methodology, Writing – review & editing. **Sergei L. Dudarev:** Conceptualization, Formal analysis, Writing – review & editing.

Declaration of competing interest

The authors declare that they have no known competing financial interests or personal relationships that could have appeared to influence the work reported in this paper.

Data availability

Data will be made available on request.

Acknowledgement

Appendix A. Supplementary material

Supplementary material related to this article can be found online at https://doi.org/10.1016/j.jnucmat.2023.154662.

References

[1] S. Sato, K. Maki, Analytical representation for neutron streaming through slits in fusion reactor blanket by Monte Carlo calculation, Fusion Eng. Des. 65 (2003) 501–524, https://doi.org/10.1016/S0920-3796(03)00003-6.

[2] L. Reali, M.R. Gilbert, M. Boleininger, S.L. Dudarev, Intense γ-photon and high-energy electron production by neutron irradiation: effects of nuclear excitations on reactor materials, PRX Energy 2 (2023) 023008, https://doi.org/10.1103/PRXEnergy.2.023008.

[3] M.R. Gilbert, J. Marian, J.-C. Sublet, Energy spectra of primary knock-on atoms under neutron irradiation, J. Nucl. Mater. 467 (2015) 121–134, https://doi.org/10.1016/j.jnucmat.2015.09.023.

[4] A.E. Sand, S.L. Dudarev, K. Nordlund, High-energy collision cascades in tungsten: dislocation loops structure and clustering scaling laws, Europhys. Lett. 103 (4) (2013) 46003, https://doi.org/10.1209/0295-5075/103/46003.

[5] D.R. Mason, A.E. Sand, X. Yi, S.L. Dudarev, Direct observation of the spatial distribution of primary cascade damage in tungsten, Acta Mater. 144 (2018) 905–917, https://doi.org/10.1016/j.actamat.2017.10.031, http://www.sciencedirect.com/science/article/pii/S1359645417308893.

[6] K. Nordlund, S.J. Zinkle, A.E. Sand, F. Granberg, R.S. Averback, R. Stoller, T. Suzudo, L. Malerba, F. Banhart, W.J. Weber, F. Willaime, S.L. Dudarev, D. Simeone, Improving atomic displacement and replacement calculations with physically realistic damage models, Nat. Commun. 9 (2018) 1084, https://doi.org/10.1038/s41467-018-03415-5.

[7] F. Hofmann, D.R. Mason, J.K. Eliason, A.A. Maznev, K.A. Nelson, S.L. Dudarev, Non-contact measurement of thermal diffusivity in ion-implanted nuclear materials, Sci. Rep. 5 (2015) 16042, https://doi.org/10.1038/srep16042.

[8] S. Cui, R.P. Doerner, M.J. Simmonds, C. Xu, Y. Wang, E. Dechaumphai, E. Fu, G.R. Tynan, R. Chen, Thermal conductivity degradation and recovery in ion beam damaged tungsten at different temperature, special Section in: 18th International Conference on Fusion Reactor Materials, J. Nucl. Mater. 511 (2018) 141–147, https://doi.org/10.1016/j.jnucmat.2018.09.002, http://www.sciencedirect.com/science/article/pii/S002231151830494X.

[9] A. Reza, H. Yu, K. Mizohata, F. Hofmann, Thermal diffusivity degradation and point defect density in self-ion implanted tungsten, Acta Mater. 193 (2020) 270–279, https://doi.org/10.1016/j.actamat.2020.03.034, https://www.sciencedirect.com/science/article/pii/S1359645420302214.

[10] G.R. Odette, G.E. Lucas, Embrittlement of nuclear reactor pressure vessels, JOM 53 (2001) 18–22, https://doi.org/10.1007/s11837-001-0081-0.

[11] A. Hasegawa, M. Fukuda, S. Nogami, K. Yabuuchi, Neutron irradiation effects on tungsten materials, in: Proceedings of the 11th International Symposium on Fusion

Nuclear Technology-11 (ISFNT-11), Barcelona, Spain, 15–20 September, 2013, Fusion Eng. Des. 89 (7) (2014) 1568–1572, https://doi.org/10.1016/j.fusengdes.2014.04.035, http://www.sciencedirect.com/science/article/pii/S0920379614003123.

[12] J. Matolich, H. Nahm, J. Moteff, Swelling in neutron irradiated tungsten and tungsten-25 percent rhenium, Scr. Metall. 8 (7) (1974) 837–841, https://doi.org/10.1016/0036-9748(74)90304-4, https://www.sciencedirect.com/science/article/pii/0036974874903044.

[13] F.A. Garner, M.B. Toloczko, B.H. Sencer, Comparison of swelling and irradiation creep behavior of fcc-austenitic and bcc-ferritic/martensitic alloys at high neutron exposure, J. Nucl. Mater. 276 (1) (2000) 123–142, https://doi.org/10.1016/S0022-3115(99)00225-1, https://www.sciencedirect.com/science/article/pii/S0022311599002251.

[14] R.A. Holt, Mechanisms of irradiation growth of alpha-zirconium alloys, J. Nucl. Mater. 159 (1988) 310–338, https://doi.org/10.1016/0022-3115(88)90099-2.

[15] J.-L. Boutard, A. Alamo, R. Lindau, M. Rieth, Fissile core and tritium-breeding blanket: structural materials and their requirements, C. R. Phys. 9 (2007) 287–302, https://doi.org/10.1016/j.crhy.2007.11.004.

[16] C. Cabet, F. Dalle, E. Gaganidze, J. Henry, H. Tanigawa, Ferritic-martensitic steels for fission and fusion applications, J. Nucl. Mater. 523 (2019) 510–537, https://doi.org/10.1016/j.jnucmat.2019.05.058.

[17] H. Gleiter, Nanocrystalline materials, Prog. Mater. Sci. 33 (4) (1989) 223–315, https://doi.org/10.1016/0079-6425(89)90001-7, https://www.sciencedirect.com/science/article/pii/0079642589900017.

[18] M. Samaras, P.M. Derlet, H. Van Swygenhoven, M. Victoria, Computer simulation of displacement cascades in nanocrystalline ni, Phys. Rev. Lett. 88 (2002) 125505, https://doi.org/10.1103/PhysRevLett.88.125505, https://link.aps.org/doi/10.1103/PhysRevLett.88.125505.

[19] N. Nita, R. Schaeublin, M. Victoria, Impact of irradiation on the microstructure of nanocrystalline materials, J. Nucl. Mater. 329–333 (2004) 953–957, https://doi.org/10.1016/j.jnucmat.2004.04.058.

[20] Y. Chimi, A. Iwase, N. Ishikawa, M. Kobiyama, T. Inami, S. Okuda, Accumulation and recovery of defects in ion-irradiated nanocrystalline gold, J. Nucl. Mater. 297 (3) (2001) 355–357, https://doi.org/10.1016/S0022-3115(01)00629-8, https://www.sciencedirect.com/science/article/pii/S0022311501006298.

[21] I.J. Beyerlein, A. Caro, M.J. Demkowicz, N.A. Mara, A. Misra, B.P. Uberuaga, Radiation damage tolerant nanomaterials, Mater. Today 16 (11) (2013) 443–449, https://doi.org/10.1016/j.mattod.2013.10.019, https://www.sciencedirect.com/science/article/pii/S1369702113003581.

[22] I.J. Beyerlein, M.J. Demkowicz, A. Misra, B. Uberuaga, Defect-interface interactions, Prog. Mater. Sci. 74 (2015) 125–210, https://doi.org/10.1016/j.pmatsci.2015.02.001.

[23] M. Dürrschnabel, M. Klimenkov, U. Jäntsch, M. Rieth, H.C. Schneider, D. Terentyev, New insights into microstructure of neutron-irradiated tungsten, Sci. Rep. 11 (1) (2021) 7572, https://doi.org/10.1038/s41598-021-86746-6.

[24] O. El-Atwani, A. Suslova, T. Novakowski, K. Hattar, M. Efe, S. Harilal, A. Hassanein, In-situ tem/heavy ion irradiation on ultrafine- and nanocrystalline-grained tungsten: effect of 3 Mev Si, Cu and W ions, Mater. Charact. 99 (2015) 68–76, https://doi.org/10.1016/j.matchar.2014.11.013, https://www.sciencedirect.com/science/article/pii/S104458031400343X.

[25] M. Rose, A. Balogh, H. Hahn, Instability of irradiation induced defects in nanostructured materials, in: Ion Beam Modification of Materials, Nucl. Instrum. Methods Phys. Res., Sect. B, Beam Interact. Mater. Atoms 127-128 (1997) 119–122, https://doi.org/10.1016/S0168-583X(96)00863-4, https://www.sciencedirect.com/science/article/pii/S0168583X96008634.

[26] S. Dey, J.W. Drazin, Y. Wang, J.A. Valdez, T.G. Holesinger, B.P. Uberuaga, R.H.R. Castro, Radiation tolerance of nanocrystalline ceramics: insights from yttria stabilized zirconia, Sci. Rep. 5 (1) (2015) 7746, https://doi.org/10.1038/srep07746.

[27] Y. Zhu, J. Luo, X. Guo, Y. Xiang, S.J. Chapman, Role of grain boundaries under long-time radiation, Phys. Rev. Lett. 120 (2018) 222501, https://doi.org/10.1103/PhysRevLett.120.222501.

[28] M.A. Tschopp, K.N. Solanki, F. Gao, X. Sun, M.A. Khaleel, M.F. Horstemeyer, Probing grain boundary sink strength at the nanoscale: energetics and length scales of vacancy and interstitial absorption by grain boundaries in α-Fe, Phys. Rev. B 85 (2012) 064108, https://doi.org/10.1103/PhysRevB.85.064108, https://link.aps.org/doi/10.1103/PhysRevB.85.064108.

[29] X.-M. Bai, A.F. Voter, R.G. Hoagland, M. Nastasi, B.P. Uberuaga, Efficient annealing of radiation damage near grain boundaries via interstitial emission, Science 327 (5973) (2010) 1631–1634, https://doi.org/10.1126/science.1183723, https://science.sciencemag.org/content/327/5973/1631.full.pdf, https://science.sciencemag.org/content/327/5973/1631.

[30] M. Jin, P. Cao, S. Yip, M.P. Short, Radiation damage reduction by grain-boundary biased defect migration in nanocrystalline Cu, Acta Mater. 155 (2018) 410–417, https://doi.org/10.1016/j.actamat.2018.05.071, https://www.sciencedirect.com/science/article/pii/S1359645418304622.

[31] M. Jin, P. Cao, M.P. Short, Mechanisms of grain boundary migration and growth in nanocrystalline metals under irradiation, Scr. Mater. 163 (2019) 66–70, https://doi.org/10.1016/j.scriptamat.2018.12.038, https://www.sciencedirect.com/science/article/pii/S1359646219300077.

[32] X. Li, W. Liu, Y. Xu, C. Liu, B. Pan, Y. Liang, Q. Fang, J.-L. Chen, G.-N. Luo, G.-H. Lu, Z. Wang, Radiation resistance of nano-crystalline iron: coupling of

[33] the fundamental segregation process and the annihilation of interstitials and vacancies near the grain boundaries, Acta Mater. 109 (2016) 115–127, https://doi.org/10.1016/j.actamat.2016.02.028, https://www.sciencedirect.com/science/article/pii/S1359645416301021.

[33] T. Frolov, Q. Zhu, T. Oppelstrup, J. Marian, R.E. Rudd, Structures and transitions in bcc tungsten grain boundaries and their role in the absorption of point defects, Acta Mater. 159 (2018) 123–134, https://doi.org/10.1016/j.actamat.2018.07.051, https://www.sciencedirect.com/science/article/pii/S1359645418305871.

[34] X.-M. Bai, B.P. Uberuaga, The influence of grain boundaries on radiation-induced point defect production in materials: a review of atomistic studies, JOM 65 (3) (2013) 360–373, https://doi.org/10.1007/s11837-012-0544-5.

[35] W.S. Yu, M.J. Demkowicz, Non-coherent Cu grain boundaries driven by continuous vacancy loading, J. Mater. Sci. 50 (11) (2015) 4047–4065, https://doi.org/10.1007/s10853-015-8961-9.

[36] C.M. Barr, E.Y. Chen, J.E. Nathaniel, P. Lu, D.P. Adams, R. Dingreville, B.L. Boyce, K. Hattar, D.L. Medlin, Irradiation-induced grain boundary facet motion: in situ observations and atomic-scale mechanisms, Sci. Adv. 8 (23) (2022) eabn0900, https://doi.org/10.1126/sciadv.abn0900, https://www.science.org/doi/pdf/10.1126/sciadv.abn0900, https://www.science.org/doi/abs/10.1126/sciadv.abn0900.

[37] D. Kaoumi, A.T. Motta, R.C. Birtcher, A thermal spike model of grain growth under irradiation, J. Appl. Phys. 104 (2008) 073525, https://doi.org/10.1063/1.2988142.

[38] P. Wang, D.A. Thompson, W.W. Smeltzer, Implantation of Ni thin films and single crystals with Ag ions, Nucl. Instrum. Methods Phys. Res., Sect. B, Beam Interact. Mater. Atoms 7–8 (1985) 97–102, https://doi.org/10.1016/0168-583X(85)90536-1.

[39] P. Wang, D.A. Thompson, W.W. Smeltzer, Implantation and grain growth in Ni thin films induced by Bi and Ag ions, Nucl. Instrum. Methods Phys. Res., Sect. B, Beam Interact. Mater. Atoms 16 (1986) 288–292, https://doi.org/10.1016/0168-583X(86)90025-X.

[40] D.C. Bufford, F.F. Abdeljawad, S.M. Foiles, K. Hattar, Unraveling irradiation induced grain growth with in situ transmission electron microscopy and coordinated modeling, Appl. Phys. Lett. 107 (2015) 191901, https://doi.org/10.1063/1.4935238.

[41] G.H. Vineyard, Thermal spikes and activated processes, Radiat. Eff. 29 (1976) 245–248, https://doi.org/10.1080/00337577608233050.

[42] P.M. Derlet, S.L. Dudarev, Microscopic structure of a heavily irradiated material, Phys. Rev. Mater. 4 (2020) 023605, https://doi.org/10.1103/PhysRevMaterials.4.023605, https://link.aps.org/doi/10.1103/PhysRevMaterials.4.023605.

[43] D.R. Mason, S. Das, P.M. Derlet, S.L. Dudarev, A.J. London, H. Yu, N.W. Phillips, D. Yang, K. Mizohata, R. Xu, F. Hofmann, Observation of transient and asymptotic driven structural states of tungsten exposed to radiation, Phys. Rev. Lett. 125 (2020) 225503, https://doi.org/10.1103/PhysRevLett.125.225503, https://link.aps.org/doi/10.1103/PhysRevLett.125.225503.

[44] S. Wang, W. Guo, T. Schwarz-Selinger, Y. Yuan, L. Ge, L. Cheng, X. Zhang, X. Cao, E. Fu, G.-H. Lu, Dynamic equilibrium of displacement damage defects in heavy-ion irradiated tungsten, Acta Mater. 244 (2022) 118578, https://doi.org/10.1016/j.actamat.2022.118578, https://www.sciencedirect.com/science/article/pii/S1359645422009533.

[45] P. Hirel, ATOMSK: a tool for manipulating and converting atomic data files, Comput. Phys. Commun. 197 (2015) 212–219, https://doi.org/10.1016/j.cpc.2015.07.012, https://www.sciencedirect.com/science/article/pii/S0010465515002817.

[46] S. Plimpton, Fast parallel algorithms for short-range molecular dynamics, J. Comput. Phys. 117 (1) (1995) 1–19, https://doi.org/10.1006/jcph.1995.1039, https://www.sciencedirect.com/science/article/pii/S002199918571039X.

[47] A.P. Thompson, H.M. Aktulga, R. Berger, D.S. Bolintineanu, W.M. Brown, P.S. Crozier, P.J. in 't Veld, A. Kohlmeyer, S.G. Moore, T.D. Nguyen, R. Shan, M.J. Stevens, J. Tranchida, C. Trott, S.J. Plimpton, LAMMPS - a flexible simulation tool for particle-based materials modeling at the atomic, meso, and continuum scales, Comput. Phys. Commun. 271 (2022) 108171, https://doi.org/10.1016/j.cpc.2021.108171, https://www.sciencedirect.com/science/article/pii/S0010465521002836.

[48] M.-C. Marinica, L. Ventelon, M.R. Gilbert, L. Proville, S.L. Dudarev, J. Marian, G. Bencteux, F. Willaime, Interatomic potentials for modelling radiation defects and dislocations in tungsten, J. Phys. Condens. Matter 25 (39) (2013) 395502, https://doi.org/10.1088/0953-8984/25/39/395502.

[49] D.R. Mason, D. Nguyen-Manh, C.S. Becquart, An empirical potential for simulating vacancy clusters in tungsten, J. Phys. Condens. Matter 29 (50) (2017) 505501, https://doi.org/10.1088/1361-648x/aa9776.

[50] A. Sand, J. Dequeker, C. Becquart, C. Domain, K. Nordlund, Non-equilibrium properties of interatomic potentials in cascade simulations in tungsten, J. Nucl. Mater. 470 (2016) 119–127, https://doi.org/10.1016/j.jnucmat.2015.12.012, https://www.sciencedirect.com/science/article/pii/S0022311515303810.

[51] F. Granberg, J. Byggmästar, K. Nordlund, Molecular dynamics simulations of high-dose damage production and defect evolution in tungsten, J. Nucl. Mater. 556 (2021) 153158, https://doi.org/10.1016/j.jnucmat.2021.153158, https://www.sciencedirect.com/science/article/pii/S0022311521003810.

[52] P.-W. Ma, D.R. Mason, S.L. Dudarev, Multiscale analysis of dislocation loops and voids in tungsten, Phys. Rev. Mater. 4 (2020) 103609, https://doi.org/10.1103/PhysRevMaterials.4.103609, https://link.aps.org/doi/10.1103/PhysRevMaterials.4.103609.

[53] M. Norgett, M. Robinson, I. Torrens, A proposed method of calculating displacement dose rates, Nucl. Eng. Des. 33 (1) (1975) 50–54, https://doi.org/10.

1016/0029-5493(75)90035-7, https://www.sciencedirect.com/science/article/pii/0029549375900357.

[54] J. Tian, H. Wang, Q. Feng, J. Zheng, X. Liu, W. Zhou, Heavy radiation damage in alpha zirconium at cryogenic temperature: a computational study, J. Nucl. Mater. 555 (2021) 153159, https://doi.org/10.1016/j.jnucmat.2021.153159, https://www.sciencedirect.com/science/article/pii/S0022311521003822.

[55] A.R. Warwick, M. Boleininger, S.L. Dudarev, Microstructural complexity and dimensional changes in heavily irradiated zirconium, Phys. Rev. Mater. 5 (2021) 113604, https://doi.org/10.1103/PhysRevMaterials.5.113604.

[56] A. Chartier, M.-C. Marinica, Rearrangement of interstitial defects in alpha-Fe under extreme condition, Acta Mater. 180 (2019) 141–148, https://doi.org/10.1016/j.actamat.2019.09.007, https://www.sciencedirect.com/science/article/pii/S1359645419305877.

[57] P. Ehrhart, P. Jung, H. Schultz, H. Ullmaier, Landolt-Börnstein - Group III Condensed Matter · Volume 25: "Atomic Defects in Metals", Springer-Verlag, Berlin Heidelberg, 1991.

[58] P.-W. Ma, S.L. Dudarev, Symmetry-broken self-interstitial defects in chromium, molybdenum, and tungsten, Phys. Rev. Mater. 3 (2019) 043606, https://doi.org/10.1103/PhysRevMaterials.3.043606, https://link.aps.org/doi/10.1103/PhysRevMaterials.3.043606.

[59] M. Ester, H.-P. Kriegel, J. Sander, X. Xu, A density-based algorithm for discovering clusters in large spatial databases with noise, in: Proceedings of the Second International Conference on Knowledge Discovery and Data Mining, AAAI Press, 1996, pp. 226–231.

[60] P.M. Larsen, S. Schmidt, J. Schiøtz, Robust structural identification via polyhedral template matching, Model. Simul. Mater. Sci. Eng. 24 (5) (2016) 055007, https://doi.org/10.1088/0965-0393/24/5/055007.

[61] W.E. Lorensen, H.E. Cline, Marching cubes: a high resolution 3d surface construction algorithm, in: Proceedings of the 14th Annual Conference on Computer Graphics and Interactive Techniques, SIGGRAPH'87, Association for Computing Machinery, New York, NY, USA, 1987, pp. 163–169.

[62] E. Chernyaev, Marching cubes 33: construction of topologically correct isosurfaces, Presented at graphicon '95, in: Graphicon 95, Saint-Petersburg, Russia 03-07.07.1995, in: Computing and Networks Division, CERN, Geneve, 1995.

[63] D.R. Mason, F. Granberg, M. Boleininger, T. Schwarz-Selinger, K. Nordlund, S.L. Dudarev, Parameter-free quantitative simulation of high-dose microstructure and hydrogen retention in ion-irradiated tungsten, Phys. Rev. Mater. 5 (2021) 095403, https://doi.org/10.1103/PhysRevMaterials.5.095403, https://link.aps.org/doi/10.1103/PhysRevMaterials.5.095403.

[64] A. Stukowski, Visualization and analysis of atomistic simulation data with OVITO–the open visualization tool, Model. Simul. Mater. Sci. Eng. 18 (1) (2009) 015012, https://doi.org/10.1088/0965-0393/18/1/015012.

[65] H. Wiedersich, On the theory of void formation during irradiation, Radiat. Eff. 12 (1972) 111–125, https://doi.org/10.1080/00337577208231128.

[66] E. Levo, F. Granberg, D. Utt, K. Albe, K. Nordlund, F. Djurabekova, Radiation stability of nanocrystalline single-phase multicomponent alloys, J. Mater. Res. 34 (5) (2019) 854–866, https://doi.org/10.1557/jmr.2019.19.

[67] W. Mohamed, B. Miller, D. Porter, K. Murty, The role of grain size on neutron irradiation response of nanocrystalline copper, Materials 9 (3) (2016), https://doi.org/10.3390/ma9030144, https://www.mdpi.com/1996-1944/9/3/144.

[68] C.M. Barr, O. El-Atwani, D. Kaoumi, K. Hattar, Interplay between grain boundaries and radiation damage, JOM 71 (4) (2019) 1233–1244, https://doi.org/10.1007/s11837-019-03386-y.

[69] X. Yi, M.L. Jenkins, M.A. Kirk, Z. Zhou, S.G. Roberts, In-situ TEM studies of 150 keV W+ ion irradiated W and W-alloys: damage production and microstructural evolution, Acta Mater. 112 (2016) 105–120, https://doi.org/10.1016/j.actamat.2016.03.051, http://www.sciencedirect.com/science/article/pii/S135964541630204X.

[70] A.R. Warwick, R. Thomas, M. Boleininger, Ö. Koç, G. Zilahi, G. Ribárik, Z. Hegedues, U. Lienert, T. Ungar, C. Race, M. Preuss, P. Frankel, S. Dudarev, Dislocation density transients and saturation in irradiated zirconium, Int. J. Plast. 164 (2023) 103590, https://doi.org/10.1016/j.ijplas.2023.103590, https://www.sciencedirect.com/science/article/pii/S0749641923000761.